





Article

Catalytic Hydrogen Evolution from H₂S Cracking over Cr_xZnS Catalyst in a Cylindrical Single-Layered Dielectric Barrier Discharge Plasma Reactor

Saba Afzal ¹, Humaira Hussain ², Muhammad Yasin Naz ^{1,*}, Shazia Shukrullah ¹, Irshad Ahmad ¹, Muhammad Irfan ³ , Salim Nasar Faraj Mursal ³, Stanislaw Legutko ⁴ , Izabela Kruszelnicka ⁵  and Dobrochna Ginter-Kramarczyk ⁵ 

¹ Department of Physics, University of Agriculture Faisalabad, Faisalabad 38040, Pakistan

² Department of Chemistry, University of Okara, Okara 56300, Pakistan

³ Electrical Engineering Department, College of Engineering, Najran University, Najran 61441, Saudi Arabia

⁴ Faculty of Mechanical Engineering, Poznan University of Technology, 60-965 Poznan, Poland

⁵ Department of Water Supply and Bioeconomy, Faculty of Environmental Engineering and Energy, Poznan University of Technology, 60-965 Poznan, Poland

* Correspondence: yasin306@uaf.edu.pk



Citation: Afzal, S.; Hussain, H.; Naz, M.Y.; Shukrullah, S.; Ahmad, I.; Irfan, M.; Mursal, S.N.F.; Legutko, S.; Kruszelnicka, I.; Ginter-Kramarczyk, D. Catalytic Hydrogen Evolution from H₂S Cracking over Cr_xZnS Catalyst in a Cylindrical Single-Layered Dielectric Barrier Discharge Plasma Reactor. *Materials* **2022**, *15*, 7426. <https://doi.org/10.3390/ma15217426>

Academic Editors: Lakshmana Reddy Nagappagari and Muthukonda Venkatakrishnan Shankar

Received: 24 September 2022

Accepted: 18 October 2022

Published: 23 October 2022

Publisher's Note: MDPI stays neutral with regard to jurisdictional claims in published maps and institutional affiliations.



Copyright: © 2022 by the authors. Licensee MDPI, Basel, Switzerland. This article is an open access article distributed under the terms and conditions of the Creative Commons Attribution (CC BY) license (<https://creativecommons.org/licenses/by/4.0/>).

Abstract: The use of non-thermal plasma technology in producing green fuels is a much-appreciated environmentally friendly approach. In this study, an Al₂O₃-supported Cr_xZnS semiconductor catalyst was tested for hydrogen evolution from hydrogen sulfide (H₂S) gas by using a single-layered dielectric barrier discharge (DBD) system. The Al₂O₃-supported Cr_xZnS catalyst (x = 0.20, 0.25, and 0.30) was produced by using a co-impregnation method and characterized for its structural and photocatalytic characteristics. The discharge column of the DBD system was filled with this catalyst and fed with hydrogen sulfide and argon gas. The DBD plasma was sustained with a fixed AC source of 10 kV where plasma produced species and UV radiations activated the catalyst to break H₂S molecules under ambient conditions. The catalyst (hexagonal-cubic-sphalerite structure) showed an inverse relationship between the band gap and the dopant concentration. The hydrogen evolution decreased with an increase in dopant concentration in the nanocomposite. The Cr_{0.20}ZnS catalyst showed excellent photocatalytic activity under the DBD exposure by delivering 100% conversion efficiency of H₂S into hydrogen. The conversion decreased to 96% and 90% in case of Cr_{0.25}ZnS and Cr_{0.30}ZnS, respectively.

Keywords: Cr-doped ZnS; photocatalysis; hydrogen sulfide; hydrogen; dielectric barrier discharge

1. Introduction

Hydrogen sulfide (H₂S) is a poisonous gas and its production is harmful to both human health and equipment [1]. Hydrogen can be produced from various raw materials like coal, water, natural gas, hydrogen sulphide, biomass and boron hydrides using various methods (electrolytic, thermal and photolytic) [2,3]. Currently, the yearly global production of hydrogen is 50 million tons and more than 95% of it is obtained from fossil fuels. The CO₂ released by fossil fuels contributes to environmental pollution [3]. Hydrogen can also be produced by cracking hydrogen sulfide (H₂S) over a suitable catalyst. Hydrogen gas is produced through different methods [4,5]. A large amount of H₂ gas is used in industrial applications, such as the production of chemicals, oils, fats, fuels, and metal reforming [6]. Currently, the Claus method is considered to be an important hydrogen-sulfide-removal technology. This technique is generally not preferred owing to its high working cost and related environmental issues. In the Claus method, hydrogen accumulating in hydrogen sulfide cannot be regained [7]. Various approaches have been proposed for the decomposition of H₂S to produce hydrogen (H₂). These methods include the thermo-chemical method, catalytic decomposition, thermal-diffusion photochemical, electrochemical, and

plasma [7,8]. In comparative economic analysis, the thermal decomposition and non-thermal plasma (NTP) methods give better results than other methods due to their lower energy cost. At very high temperatures, the decomposition of H_2S is very low due to the limitation of the thermodynamic equilibrium. The conventional catalysts do not play a better role in converting H_2S in thermal catalytic decomposition because H_2S shows high catalytic reactivity with metal species at elevated temperatures [9]. The NTP technique has been suggested as a potential alternative for the direct decomposition of H_2S into S and H_2 , particularly due to the accomplishment of high-electron energies within a short time. In NTP, various methods have been used to breakdown H_2S . Such methods include corona, dielectric barrier discharge plasma, microwave, rotating glow, radio frequency discharge, and gliding arc discharge.

A review of the literature shows that many catalyst-hybrid systems have been investigated for the decomposition of H_2S in DBD plasma with Al_2O_3 . In addition to Al_2O_3 -supported $\text{Zn}_{0.4}\text{Cd}_{0.6}\text{S}$, ZnS and CdS have also been used for hydrogen production. The ZnS and CdS showed H_2S conversion corresponding to 90.9% and 97.9%. On the other hand, $\text{Zn}_{0.4}\text{Cd}_{0.6}\text{S}$ showed 100% catalytic activity for hydrogen production. However, it is a time-consuming catalyst and took 100 h to complete the process. Some other catalysts were also used with Al_2O_3 support to produce H_2 , such as $\text{Zn}_x\text{Cd}_{1-x}\text{S}$, $\text{MoS}_2/\text{Al}_2\text{O}_3$, La_xMnO_3 , and Mn_2O_3 . The catalytic performance of these catalysts was checked within 50 to 100 h with 100%, 99%, 52%, and 100% H_2S conversion, respectively [10,11]. A similar activity of H_2 production was also observed when Zhao et al. [10] used the Al_2O_3 -supported Cr_xZnS semiconductor. They used different molar ratios of Cr/Zn ($x = 0.10, 0.15, 0.20$ and 0.25) in their investigations. These molar ratios resulted in 81.8%, 87.4%, 100% and 89.7% conversion of H_2S , respectively [12–14].

The Cr-doped ZnS exhibits high-catalytic activity compared to transition metal-doped ZnS . Barnhart et al. [13] reported that Cr is the 21st most common element in the Earth's crust, with a concentration of 100 ppm. Poornaprakash et al. [14] explained that chromium is an important metal that has an abundant shell structure. Moreover, due to the closed ionic radius of Cr^{3+} (0.63 Å) and Zn^{2+} (0.74 Å), it is easy for Cr^{3+} to substitute Zn^{2+} and penetrate into the host lattice of ZnS . On the other hand, ZnS also acts as a host material with its bulky band gap (3.67 eV). Due to its low toxicity and low cost, it produces different nanostructures in various research applications. In this research, H_2 gas was produced from Cr-doped ZnS by non-thermal plasma treatment at atmospheric pressure. This method consumed a very small amount of energy at low temperatures when a catalyst was placed in the quartz discharge tube. The catalyst (Cr_xZnS) was prepared by the co-impregnation/wet impregnation method with different molar ratios of Cr/Zn ($x = 0.20, 0.25$, and 0.30). The advantage of this method is that a layer of active matter can easily be prepared on the catalyst surface. Different characterization techniques such as X-ray diffraction (XRD), Ultraviolet-visible (UV-Vis) spectroscopy, Fourier transform infrared spectroscopy (FTIR) and Scanning transmission electron microscopy (STEM) was used to analyze the catalysts. These analyses gave information about the structure, crystal planes, band gap, and light absorbance. The previously reported methods were time-consuming and energy-intensive compared to our work. This study produced reasonably good results in relatively shorter periods. The $\text{Cr}_{0.20}\text{ZnS}$ showed 100% production of H_2 within 15 h of the process.

2. Experimental Part

2.1. Chemicals

All the chemicals, including zinc sulfide (ZnS), gamma-aluminum oxide ($\gamma\text{-Al}_2\text{O}_3$), zinc nitrate $\text{Zn}(\text{NO}_3)_2$, and chromium nitrate $\text{Cr}(\text{NO}_3)_3$ were supplied by Merck & Co., Inc. (Rahway, NJ, USA).

2.2. Preparation of Photocatalyst

The procedure of synthesis of photocatalyst is illustrated in Figure 1. Using the illustrated procedure, a series of Cr-doped ZnS with Al_2O_3 support was prepared with

different ratios of chromium (Cr). A wet-impregnation method was adopted to prepare the catalyst samples. In this method, the ZnS amount was taken as 15 g, which is 10 wt% of γ - Al_2O_3 . An aqueous solution was prepared by adding 5 g of a Zn-nitrate solution to 15 mL of distilled water. The Cr-nitrate and Zn-nitrate were mixed with different molar ratios (0.20, 0.25, and 0.30) by comparing the previous research. The prepared solution and γ - Al_2O_3 were mixed with a gentle shake. The mixture was filtered by a filtration process and then dried at 120 °C for 12 h in the oven. The calcination of the material was performed in the furnace for 5 h. A fine powder was formed after crushing the calcinated material. The sulfide catalysts were formed when oxide precursors were sulfidated in the presence of sulfiding gas. Eventually, Cr_xZnS catalysts ($x = 0.20, 0.25, \text{ and } 0.30$) was prepared.

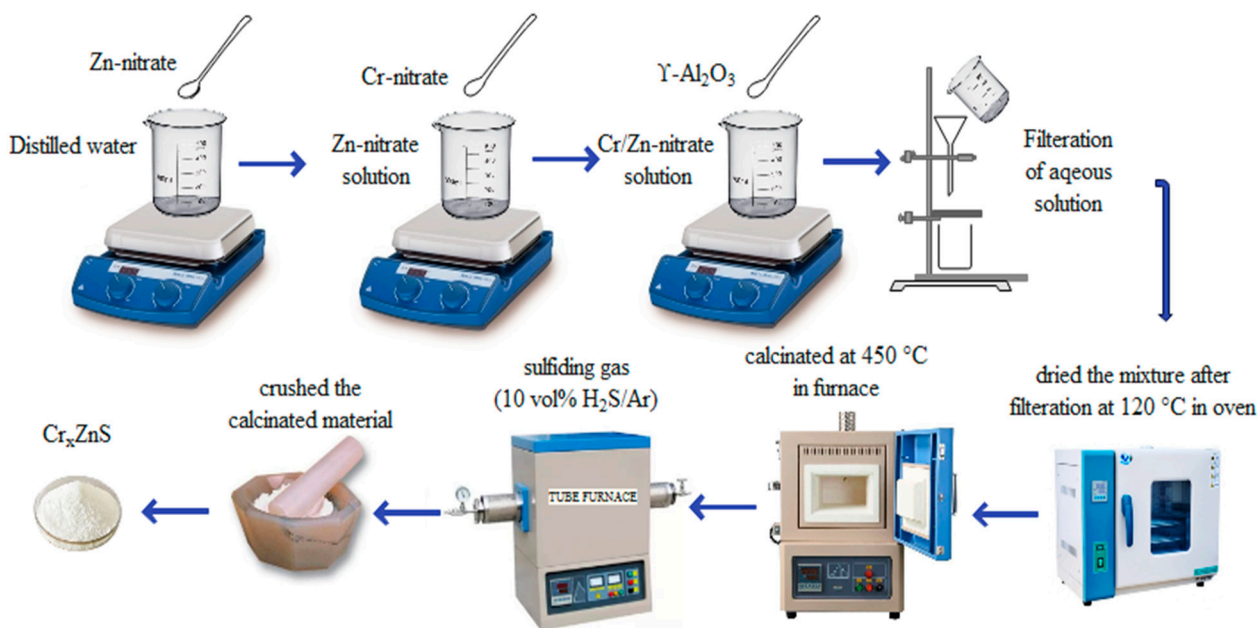


Figure 1. Illustration of the catalyst preparation procedure.

2.3. DBD Plasma-Assisted Hydrogen Evolution

The schematic and photographic views of the DBD setup, used for the production of hydrogen by cracking H_2S molecules over the composite catalyst, are given in Figure 2. This laboratory-built system consists of a 30 cm DBD vertical column with an active plasma column length of 23 cm. A quartz tube with a 4 mm wall thickness and a 12 mm internal diameter was used as a DBD column. A copper rod of 8 mm diameter was passed through the tube to work as one of the two electrodes. The tube was wrapped with a copper wire to work as an electrode for uniform radial and spatial distribution of the applied power and plasma. The upper end of the tube was used as a gas inlet and the lower end was connected with the gas analyzer. The discharge column of the DBD system was filled with this catalyst and fed with hydrogen-sulfide and argon gas.

The DBD plasma was sustained with a fixed AC source of 10 kV where plasma-produced species and UV radiations were used to activate the catalyst to break the H_2S molecules under ambient conditions. The Al_2O_3 -supported Cr_xZnS semiconductor catalyst was tested for hydrogen evolution from H_2S gas using this single-layered DBD system [15]. The discharge volume of the dielectric-barrier-discharge reactor was 22 mL [16]. One end of the battery was attached to the wire and the other to the rod. About 10 g of the Cr_xZnS catalyst ($x = 0.20, 0.25, \text{ and } 0.30$) was loaded in the discharge column. At the same time, the gas ($\text{Ar} + \text{H}_2\text{S}$) was passed through the loaded column. The gas product of the reaction in

the discharge column was analyzed. The relationship between the H_2S ($X_{\text{Hydrogen sulfide}}$) and H_2 yield (X_{Hydrogen}) is shown as follows:

$$X_{\text{Hydrogen sulfide}} = X_{\text{Hydrogen}} + \frac{A}{A_0} \times 100\% \quad (1)$$

where A is the value of the H_2 peak area of effluence. A_0 has represented the hydrogen peak area at 100% hydrogen sulfide conversion. The area of the represents the energy lost during a single voltage cycle in the discharge. The total input energy used in the plasma during the process was calculated by the specific input energy (SIE) as:

$$\text{SIE} = \frac{P}{V} \quad (2)$$

where V is the flowrate of gas (L/s) and P is the discharge power (W). The energy utilization for the H_2 generation (E , eV) was calculated from the specific input energy as:

$$\text{Energy consumption (E, eV)} = \frac{P_{\text{discharge}}}{\text{H}_2\text{S converted (mol/s)}} \times \frac{1}{96} \quad (3)$$

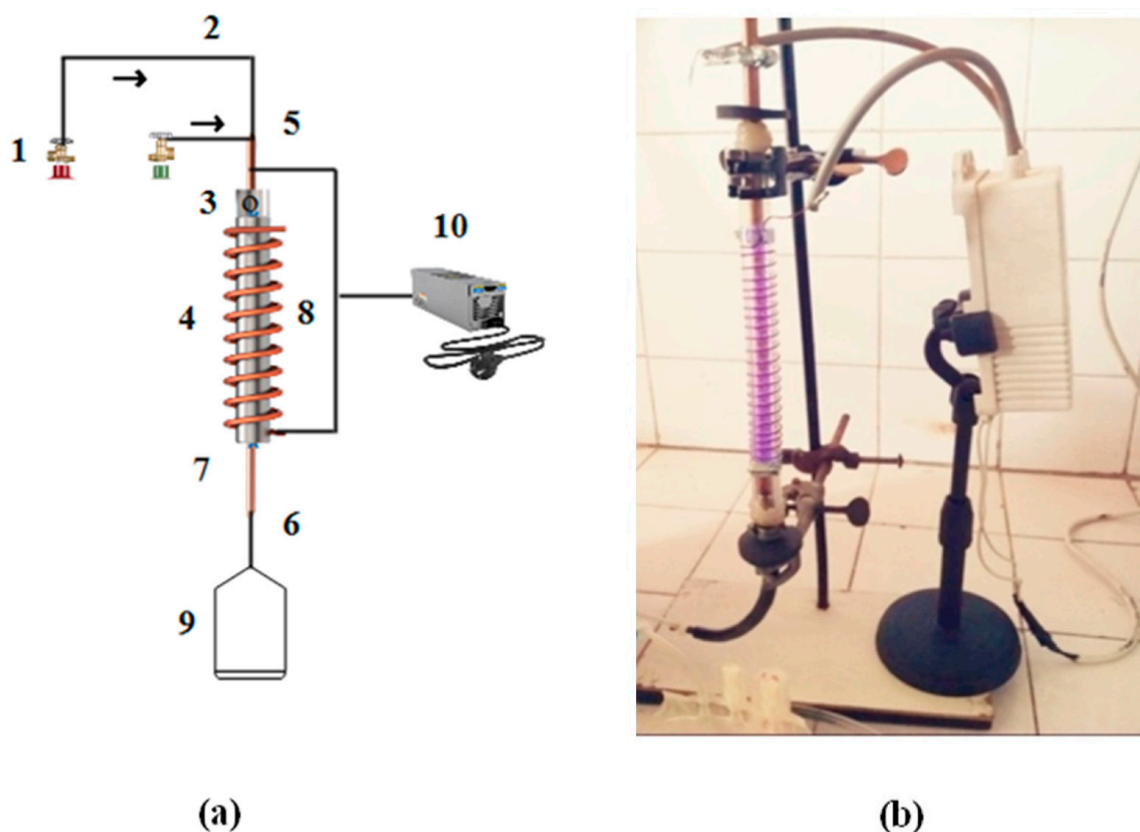


Figure 2. (a) Schematic of DBD plasma system. (1) Gas cylinder, (2) Gas supply, (3) Hole in rod, (4) Quartz tube, (5) Inlet, (6) Outlet, (7) Inner electrode, (8) Copper coil, (9) Gas sampling bag, and (10) AC power supply. The arrows indicate the direction of the gas flow (H_2S and Ar). (b) Photographic view of single-layered DBD plasma system for H_2S decomposition.

3. Results and Discussion

3.1. FTIR Analysis of Catalyst

With the Fourier transform infrared (FTIR) analysis, the absorbance of the species in the crystal surface and the nanoparticle formation of ZnS were checked. It is reported that this analysis also gives information about the chemical bonding of the chemical [17].

The FTIR absorbance spectra of Cr_xZnS with different molar ratios are shown in Figure 3. As shown in Table 1, FTIR analysis showed the same peaks for Cr_xZnS samples with different ratios ($x = 0.20, 0.25$, and 0.30) within the range of $500\text{--}4000\text{ cm}^{-1}$. The FTIR peaks were located around 3700 cm^{-1} , 1588 cm^{-1} , 1531 cm^{-1} , and 1020 cm^{-1} . All the peaks exist in the group frequency region (GFR) except 1020 cm^{-1} because its range was lower than the other three peaks, so it was observed in the fingerprint region (FPR) [18]. The peak at 3700 cm^{-1} was due to O—H stretching vibration. This peak shows an alcohol group of compounds with intermolecular forces based on their structure [19]. The peaks at 1588 cm^{-1} and 1020 cm^{-1} exhibited the same amines groups with no intermolecular force at medium peaks. Both peaks have different vibrations, i.e., 1588 cm^{-1} represents the N—H bending due to GFR and 1020 cm^{-1} represents the C—N stretching vibration in FPR. There is a strong peak appearance at 1531 cm^{-1} caused by N—O stretching. It exists in a nitro-compound group with no bonding forces.

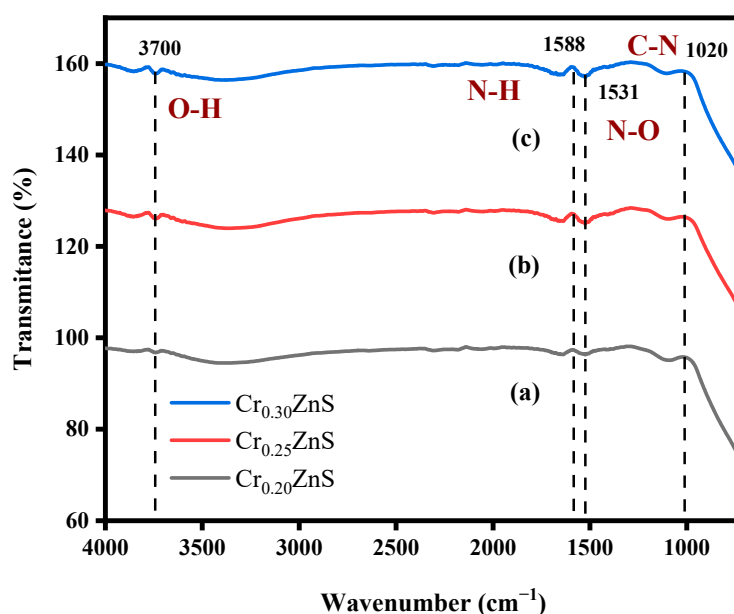


Figure 3. FTIR spectra of (a) $\text{Cr}_{0.20}\text{ZnS}$, (b) $\text{Cr}_{0.25}\text{ZnS}$, and (c) $\text{Cr}_{0.30}\text{ZnS}$ catalyst samples.

Table 1. FTIR peaks and corresponding groups of the Cr_xZnS catalyst.

FTIR peaks	Spectrum region	Appearance	Bonding force	Group	Compound class
3700	GFR	medium, sharp	intermolecular	O—H stretching	alcohol
1588	GFR	medium	-	N—H bending	amines
1531	GFR	strong	-	N—O stretching	nitro-compound
1020	FPR	medium	-	C—N stretching	amines

3.2. UV-Visible Analysis

The absorption spectra of catalysts Cr_xZnS ($x = 0.20, 0.25$, and 0.30) were examined by UV-Vis analysis within the wavelength range of 200 nm to 800 nm and obtained results are shown in Figure 4. The absorption edges at 367 nm , 376 nm , and 379 nm correspond to $\text{Cr}_{0.20}\text{ZnS}$, $\text{Cr}_{0.25}\text{ZnS}$, and $\text{Cr}_{0.30}\text{ZnS}$ respectively observed along the x-axis [20]. In Figure 5, the $\text{Cr}_{0.30}\text{ZnS}$ catalyst showed a superior shift in absorption edge (red-shift) towards the visible light region in contrast to other samples, showing a maximum absorption upto

379 nm [21,22]. $\text{Cr}_{0.20}\text{ZnS}$, $\text{Cr}_{0.25}\text{ZnS}$ and $\text{Cr}_{0.30}\text{ZnS}$ catalysts represented the absorbance values of 0.162 nm, 0.324 nm and 0.563 nm, respectively. Bodke et al. [14] reported that the concentration of doped Cr^{3+} had a pronounced effect on the optical properties of the ZnS catalyst and witnessed a significant red-shift in the absorption of Cr-doped ZnS.

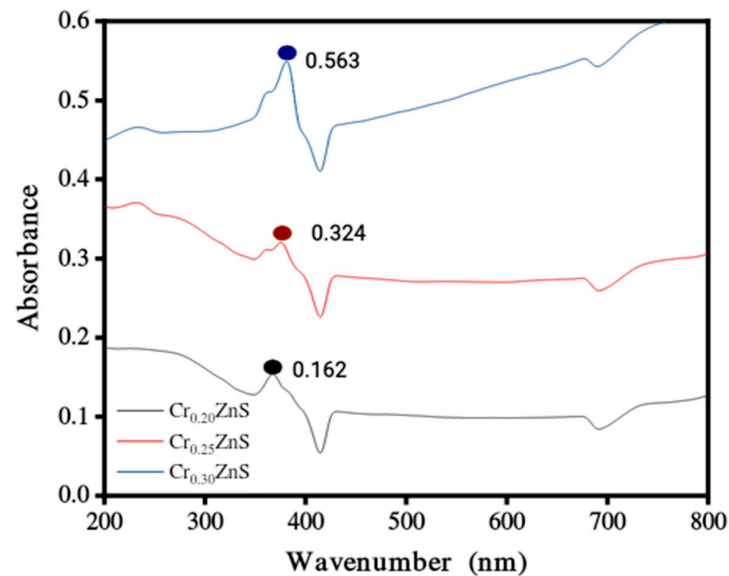


Figure 4. UV-Vis absorbance spectra of Cr_xZnS ($x = 0.20, 0.25$, and 0.30) catalyst.

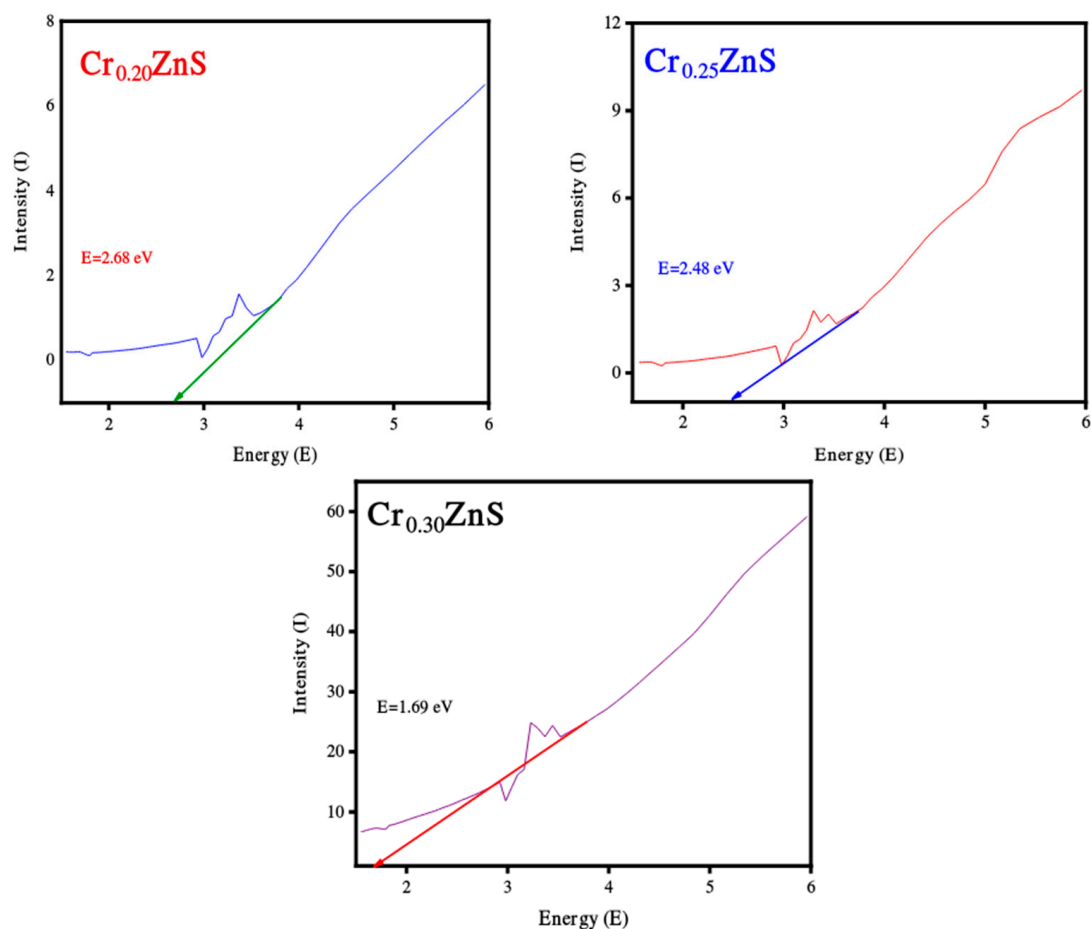


Figure 5. Band gap estimation of $\text{Cr}_{0.20}\text{ZnS}$, $\text{Cr}_{0.25}\text{ZnS}$, and $\text{Cr}_{0.30}\text{ZnS}$ catalyst samples.

The band gap values of the catalysts with different Cr compositions are reported in Figure 5. The band gap of Cr_xZnS with $x = 0.20, 0.25$, and 0.30 was found to be 2.68, 2.48, and 1.69 eV, respectively. These band gap values are lower than the standard value of bulk ZnS (3.6 eV) [23].

3.3. X-ray Diffraction Analysis

The XRD analysis of as-synthesized catalysts Cr_xZnS ($x = 0.20, 0.25$, and 0.30) are shown in Figure 6. All prepared samples showed similar diffraction peaks, identifying no variation in the host crystal structure after introducing Cr^{3+} ions into its lattice. The different diffraction peaks were found at 2θ values of $31^\circ, 36^\circ, 47^\circ$, and 56° , which correspond to (002), (001), (110), and (112) planes of ZnS, respectively. There was no other obvious indication of any other diffraction peak found except for the alumina peak. Among all samples, only the $\text{Cr}_{0.20}\text{ZnS}$ catalyst showed the origination of diffraction peak related to Cr impurity [24]. The information about the existence of the characteristic peak of (110) plane was confirmed from JCPDS#65-0309. The crystal structure of the Cr_xZnS catalyst is cubic sphalerite.

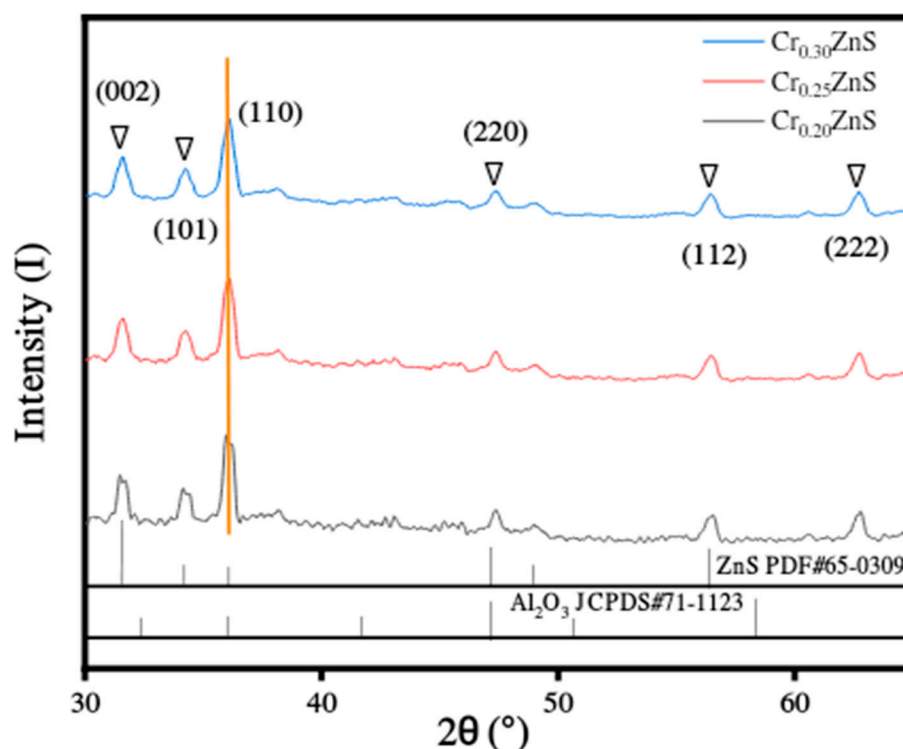


Figure 6. XRD spectra of the Cr_xZnS ($x = 0.20, 0.25$, and 0.30) catalyst.

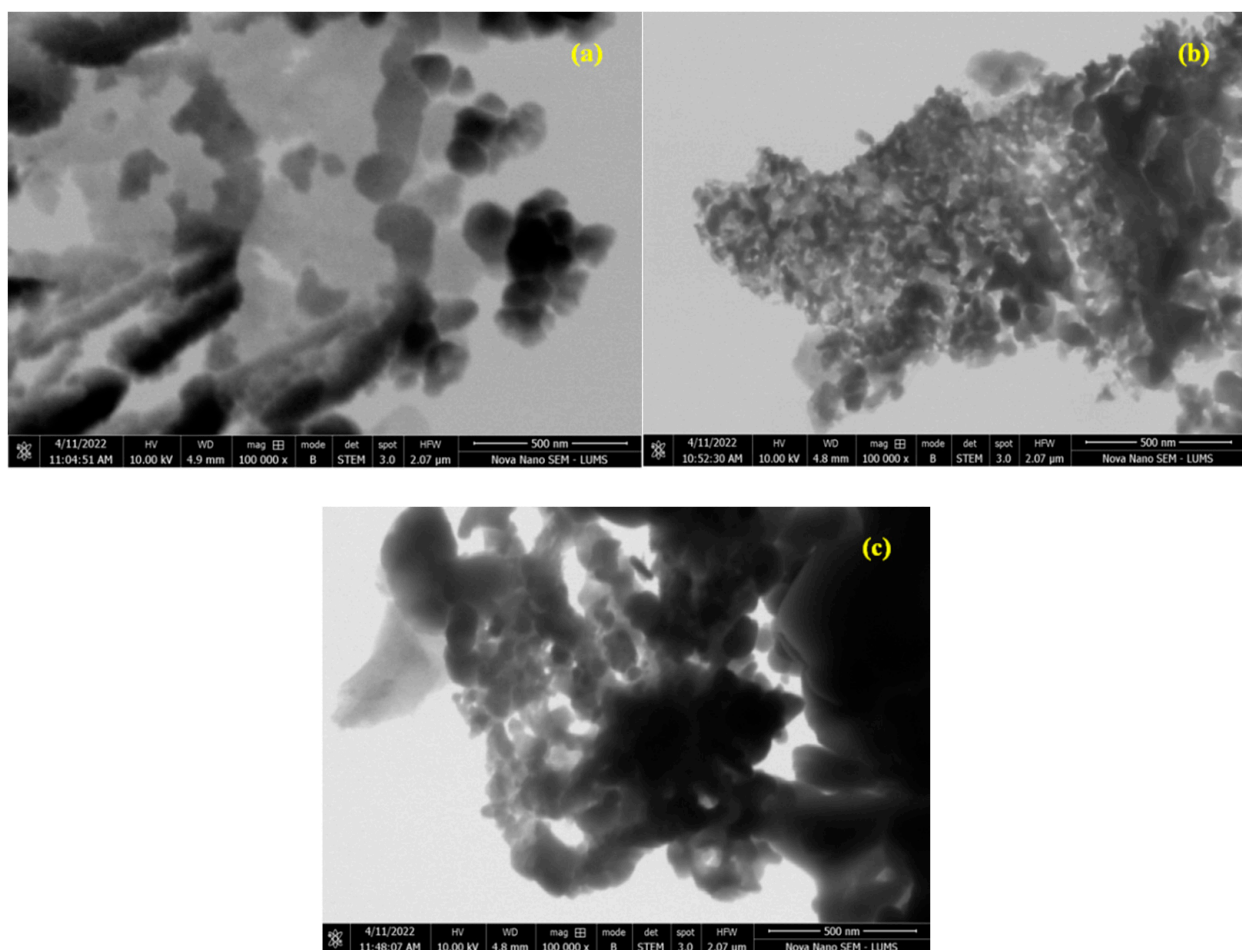
The surface area decreased with an increase in a molar ratio of Cr/Zn. Ramasamy [25] reported that the lattice constants were reduced with Cr doping because of the ionic radius (0.63 \AA and 0.74 \AA) of Cr^{3+} and Zn^{2+} ions. In our study, as the Cr^{3+} content increased, the lattice parameters were decreased in the case of all as-prepared Cr_xZnS catalysts. The Scherrer equation was used to calculate the average crystallite size of the catalyst. The grain sizes of Cr_xZnS were estimated to be 18.30, 17.89, and 17.49 nm, corresponding to the $\text{Cr}_{0.20}\text{ZnS}$, $\text{Cr}_{0.25}\text{ZnS}$, and $\text{Cr}_{0.30}\text{ZnS}$, respectively. Since the band gap and the grain size are inversely related to each other; therefore, our measured band gap and crystallite size are in good agreement, as illustrated in Table 2 [26].

Table 2. The band gap and grain size of Cr_xZnS catalyst samples.

Catalyst	FWHM	Grain size (nm)	Band gap (eV)
$\text{Cr}_{0.20}\text{ZnS}$	0.477	18.30	2.68
$\text{Cr}_{0.25}\text{ZnS}$	0.488	17.89	2.48
$\text{Cr}_{0.30}\text{ZnS}$	0.499	17.49	1.69

3.4. STEM Morphology Analysis

The morphology of the as-prepared samples was analyzed using the STEM technique and the results are displayed in Figure 7. The STEM analysis confirmed the successful formation of nanoparticles. The fine doping of the catalyst at a ratio of $x = 0.30$ appeared as a dark area in the images. A rough spherical morphology of the particles was observed in STEM images [27].

**Figure 7.** STEM images of (a) $\text{Cr}_{0.20}\text{ZnS}$, (b) $\text{Cr}_{0.25}\text{ZnS}$, and (c) $\text{Cr}_{0.30}\text{ZnS}$ catalyst samples.

The statistical distribution of Cr_xZnS ($x = 0.20, 0.25$, and 0.30) is expressed within the range of 1–10 nm [28]. Figure 8 shows the distribution of particle sizes measured from the STEM images. The average particle size of $\text{Cr}_{0.20}\text{ZnS}$, $\text{Cr}_{0.25}\text{ZnS}$, and $\text{Cr}_{0.30}\text{ZnS}$ was measured at about 82 nm, 79 nm, and 76 nm, respectively.

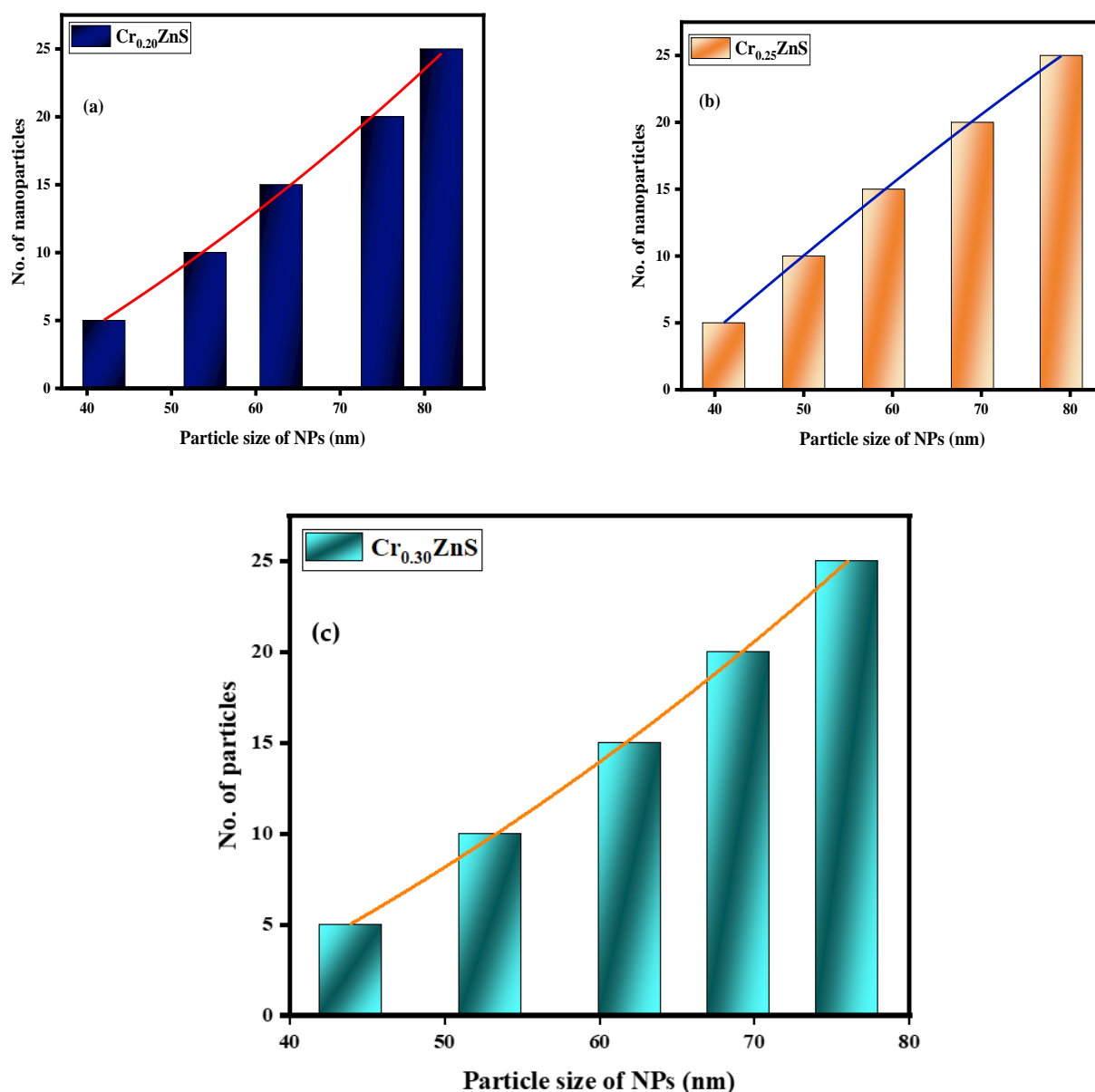


Figure 8. Particle size distribution of (a) $\text{Cr}_{0.20}\text{ZnS}$, (b) $\text{Cr}_{0.25}\text{ZnS}$, and (c) $\text{Cr}_{0.30}\text{ZnS}$ catalyst samples.

3.5. Photoluminescence Analysis

The catalysts were further characterized with PL technique to determine the extent of the photoinduced electron-hole recombination rate. Principally, high-PL-emission intensity represents the rapid recombination of charge carriers and vice versa [29]. Figure 9 shows the PL emission spectra of Cr_xZnS catalyst samples measured at room temperature and an exciton wavelength of 325 nm. The Cr doping has successfully altered the surface of the ZnS and promoted the migration of surface carriers, causing an increment in light-harvesting, which is consistent with the UV-Vis results [30]. The Cr_xZnS ($x = 0.20$) catalyst demonstrated the lowest emission intensity compared to the other two catalysts, identifying its effective suppression of charge carriers. It is worth mentioning that the PL intensity was reduced with Cr doping in the UV and visible zone because of the effective role of Cr^{3+} ions in trapping the electrons to prolong their recombination with holes [31]. Additionally, Cr^{3+} dopants provide electrons reaching the surface of the ZnS to effectively initiate the reaction to accelerate the photocatalytic process [32]. Hence, it is concluded that the PL intensity is reduced owing to a strongly inhibited recombination of photoinduced charge

carriers because Cr^{3+} captured the electrons. The Cr_xZnS ($x = 0.20$) catalyst demonstrated the least intensity; therefore, it is more appropriate for hydrogen production.

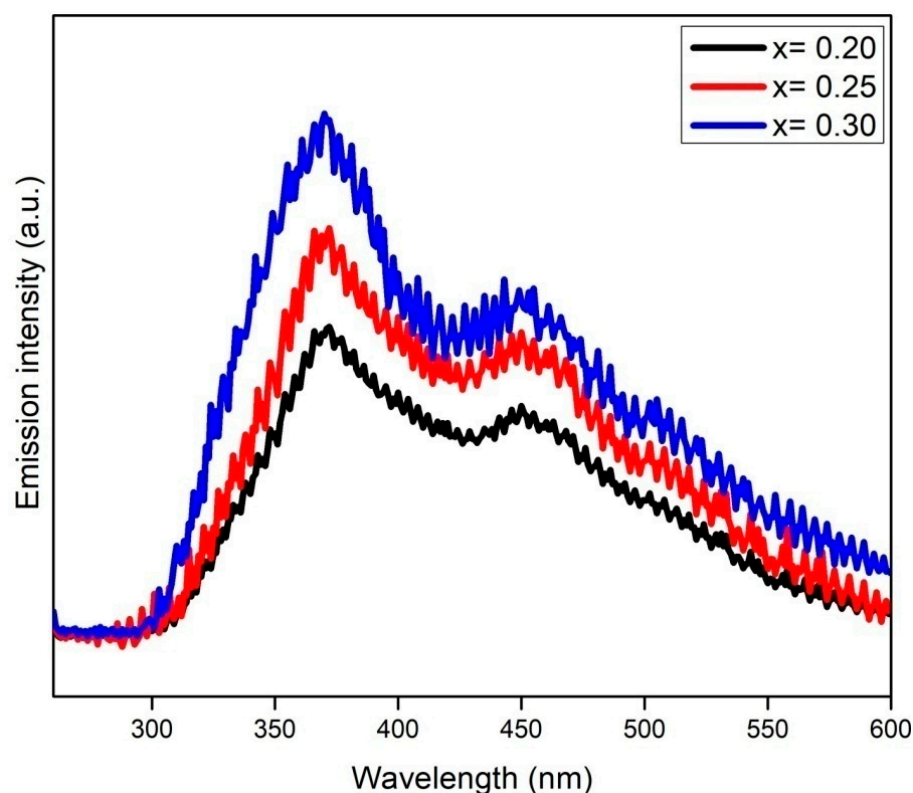


Figure 9. PL spectra of the Cr_xZnS ($x = 0.20, 0.25$, and 0.30) catalyst.

3.6. Hydrogen Evolution Activity

The catalytic performance of the Cr_xZnS catalyst samples was evaluated for hydrogen production under non-thermal plasma treatment. The catalytic performance of un-doped ZnS and Al_2O_3 as a support material was also presented. The decomposition of H_2S over the tested catalyst compositions in a single-layered DBD plasma environment is reported in Figure 10. In the case of Al_2O_3 support, both discharge diffusion and plasma-produced reactive species may be influenced. The residence time of these species may be extended by the adsorption capacity of the Al_2O_3 support [33]; however, in the literature, the electric field was enhanced by using porous materials. Both the discharge and prolonged residence time are useful for H_2S decomposition [34]. More micro-discharges occurred in the Al_2O_3 -filled gap, which led to the beginning of chemical processes involving H_2S molecules, radicals, and electrons. All prepared Cr_xZnS catalysts showed better performance of H_2S conversion than that of pure ZnS and Al_2O_3 support. The Cr_xZnS catalyst with a molar ratio of $x = 0.20$ showed the highest decomposition of H_2S .

The results after comparison revealed that H_2S conversion varied for different Cr/Zn molar ratios. The catalytic activity greatly depends upon the dopant concentration. The H_2S conversion levels significantly impact the energy needed to break down its molecules [35]. The $\text{Cr}_{0.20}\text{ZnS}$ catalyst outperformed the other tested catalysts in terms of catalytic performance and fully converted H_2S at significantly lower energies. The H_2S decomposition was 100%, 96%, and 90% when the gap was filled with $\text{Cr}_{0.20}\text{ZnS}$, $\text{Cr}_{0.25}\text{ZnS}$, and $\text{Cr}_{0.30}\text{ZnS}$, respectively. The characterization of the catalyst showed that physical and chemical properties changed with Cr/Zn molar ratio. The cubic sphalerite structure of the catalyst was shown by XRD analysis [36,37]. Cr^{3+} ions of chromium revealed uniformly scattering over the ZnS without introducing separated impurity phases.

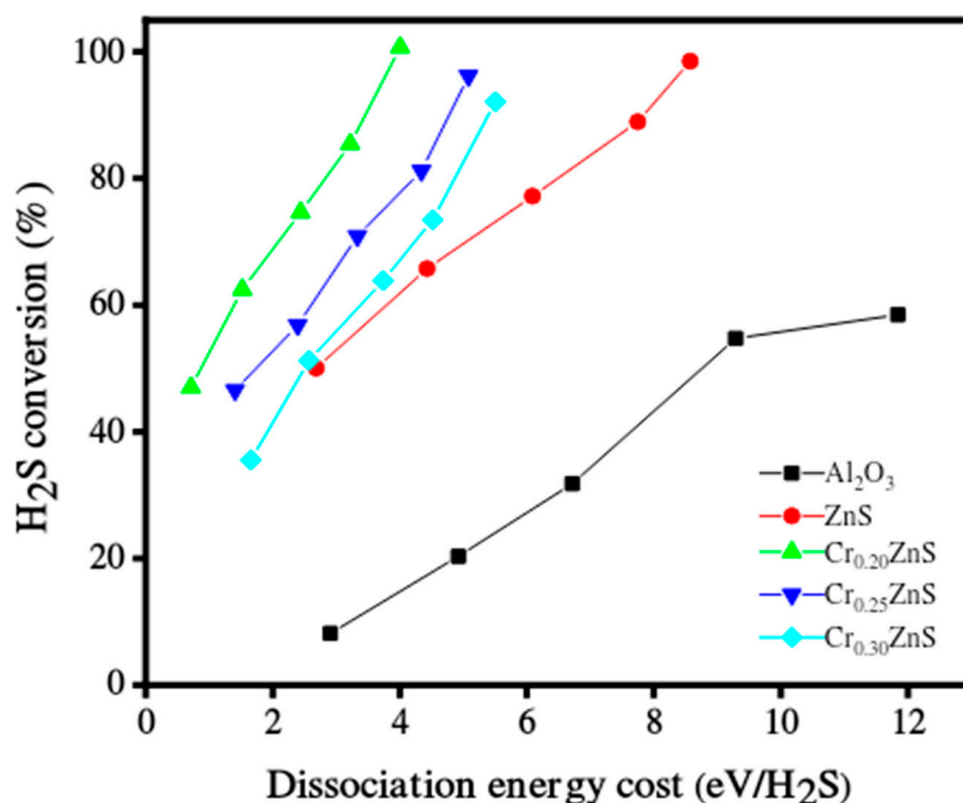


Figure 10. Hydrogen sulfide decomposition over the catalyst in DBD plasma environment.

The H₂S conversion with specific input energy varies for different H₂S concentrations over the Cr_{0.20}ZnS catalyst. The conversion rate was higher at the lower H₂S concentrations. H₂S decomposition increased with increasing the specific input energy. Chivers and Lau [36] showed similar results for the H₂S conversion under non-thermal plasma conditions. When a large number of electrons collide with Ar balance gas at lower H₂S concentrations, air balance gas is also crucial to the breakdown. Cr_{0.20}ZnS was selected to evaluate the stability of the catalytic after 100% decomposition of H₂S [38]. The long-term H₂S conversion reaction of the Cr_{0.20}ZnS catalyst is shown in Figure 11. The H₂ evaluation shows a maximum value up to 15 h and thereafter starts to decrease over time. Three different readings were noted at different time periods. The H₂ evolution decreased from 100% to 94% over the Cr_{0.20}ZnS after 22 h of reaction time. A decrease in H₂ production over time might be due to the deactivation of the catalyst.

Table 3 summarizes the findings of hydrogen production efficiency over the Cr_xZnS catalyst samples. The H₂ production during the conversion of H₂S was 100%, 96%, and 90% for $x = 0.20, 0.25$, and 0.30 , respectively. Different energy conversion was observed with the same SIE (specific input energy) values for all catalysts.

Table 3. Conversion efficiency, specific input energy, and energy consumption for catalytic hydrogen production.

Catalyst	H ₂ S conversion (%)	SIE (J/L)	Energy consumption (eV)
Cr _{0.20} ZnS	100	14.66	0.120
Cr _{0.25} ZnS	96	14.66	0.124
Cr _{0.30} ZnS	90	14.66	0.138

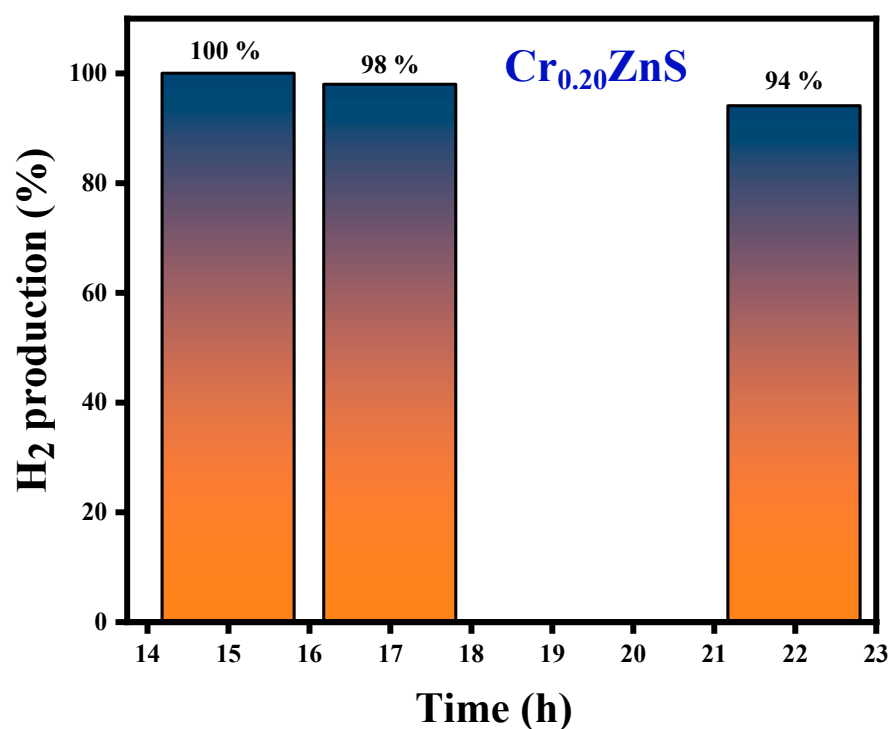


Figure 11. H₂ production of the Cr_{0.20}ZnS catalyst with time.

4. Conclusions

This laboratory-built non-thermal plasma system with a vertical DBD column was used to decompose H₂S over the Cr_xZnS catalyst for the production of hydrogen gas. The catalyst was prepared using the co-impregnation method. A FTIR spectrum showed the materials' absorbance in different regions (fingerprint and group frequency region) and functional groups. X-ray diffraction displayed the surface morphology of the catalyst. The values of intensity, millar indices, grain size, and d-spacing were decreased with increasing the Cr concentration. Hydrogen evolution was maximized (100%) after 15 h of reaction over the Cr_{0.20}ZnS. Hydrogen evolution then decreased to 94% after 22 h of reaction time, showing a decrease in catalytic activity over time. The Cr_{0.20}ZnS, Cr_{0.25}ZnS, and Cr_{0.30}ZnS catalysts showed 100%, 96%, and 90% conversion, respectively, after 15 h of processing time. The earlier reported works are time-consuming and energy-intensive compared to our work. This study produced reasonably good results in relatively shorter periods. The Cr_{0.20}ZnS showed 100% conversion of H₂S within 15 h of the process.

Author Contributions: Conceptualization, M.Y.N. and M.I.; data curation, S.A.; formal analysis, H.H., I.A. and D.G.-K.; funding acquisition, M.I.; investigation, S.S. and I.K.; methodology, H.H., S.S. and I.A.; validation, S.N.F.M.; visualization, S.L.; writing—original draft, S.A. and M.Y.N.; writing—review & editing, S.N.F.M., S.L., I.K. and D.G.-K. All authors have read and agreed to the published version of the manuscript.

Funding: The paper fee was paid through the Poznan University of Technology—project no. 0713/SBAD/0958.

Institutional Review Board Statement: No applicable.

Informed Consent Statement: No applicable.

Data Availability Statement: Data is available from the authors on reasonable request.

Acknowledgments: The authors acknowledge the support from the Deanship of Scientific Research, Najran University, Kingdom of Saudi Arabia, for funding this work under the Research Collaboration funding program grant code number NU/RC/SERC/11/4.

Conflicts of Interest: There is not known conflict of interest for publishing this work.

References

- Thangam, N.; Suganya Devi, B.; Lalitha Muthu, A.C. Hydrogen production from Hydrogen Sulfide Waste stream using Ru/Cd_{0.6}Zn_{0.4}S Photocatalyst. *Int. J. New Technol. Res.* **2015**, *1*, 4–10.
- Liao, J.; Shao, Y.; Feng, Y.; Zhang, J.; Song, C.; Zeng, W.; Tang, J.; Dong, H.; Liu, Q.; Li, H. Interfacial charge transfer induced dual-active-sites of heterostructured Cu_{0.8}Ni_{0.2}WO₄ nanoparticles in ammonia borane methanolysis for fast hydrogen production. *Appl. Catal. B Environ.* **2022**, *320*, 121973. [\[CrossRef\]](#)
- Feng, Y.; Li, Y.; Liao, Q.; Zhang, W.; Huang, Z.; Chen, X.; Shao, Y.; Dong, H.; Liu, Q.; Li, H. Modulation the electronic structure of hollow structured CuO-NiCo₂O₄ nanosphere for enhanced catalytic activity towards methanolysis of ammonia borane. *Fuel* **2022**, *332*, 126045. [\[CrossRef\]](#)
- Reddy, D.A.; Murali, G.; Vijayalakshmi, R.P.; Reddy, B.K. Room-temperature ferromagnetism in EDTA capped Cr-doped ZnS nanoparticles. *Appl. Phys. A* **2011**, *105*, 119–124. [\[CrossRef\]](#)
- Deshmukh, G.M.; Shete, A.; Pawar, D.M. Oxidative absorption of hydrogen sulfide using an iron-chelate based process: Chelate degradation. *J. Chem. Technol. Biotechnol.* **2013**, *88*, 432–436. [\[CrossRef\]](#)
- Zhao, L.; Wang, Y.; Li, X.; Wang, A.; Song, C.; Hu, Y. Hydrogen production via decomposition of hydrogen sulfide by synergy of non-thermal plasma and semiconductor catalysis. *Int. J. Hydrogen Energy* **2013**, *38*, 14415–14423. [\[CrossRef\]](#)
- Zaman, J.; Chakma, A. Production of hydrogen and sulfur from hydrogen sulfide. *Fuel Processing Technol.* **1995**, *41*, 159–198. [\[CrossRef\]](#)
- Feng, Y.; Zhang, X.; Shao, Y.; Chen, X.; Wang, H.; Li, J.; Wu, M.; Dong, H.; Liu, Q.; Li, H. Modulating the Acidic Properties of Mesoporous Mo_x-Ni_{0.8}Cu_{0.2}O Nanowires for Enhanced Catalytic Performance toward the Methanolysis of Ammonia Borane for Hydrogen Production. *ACS Appl. Mater. Interfaces* **2022**, *14*, 27979–27993. [\[CrossRef\]](#)
- Duan, L.B.; Zhao, X.R.; Liu, J.M.; Wang, T.; Rao, G.H. Room-temperature ferromagnetism in lightly Cr-doped ZnO nanoparticles. *Appl. Phys. A* **2010**, *99*, 679–683. [\[CrossRef\]](#)
- Zhao, L.; Liu, X.; Mu, X.; Li, Y.; Fang, K. Highly selective conversion of H₂S–CO₂ to syngas by combination of non-thermal plasma and MoS₂/Al₂O₃. *J. CO₂ Util.* **2020**, *37*, 45–54. [\[CrossRef\]](#)
- Eyasu, A.; Yadav, O.P.; Bachheti, R.K. Photocatalytic degradation of methyl orange dye using Cr-doped ZnS nanoparticles under visible radiation. *Int. J. Chem. Tech. Res.* **2013**, *5*, 1452–1461.
- Poornaprakash, B.; Naveen Kumar, K.; Chalapathi, U.; Reddeppa, M.; Poojitha, P.T.; Park, S.H. Chromium doped ZnS nanoparticles: Chemical, structural, luminescence and magnetic studies. *J. Mater. Sci. Mater. Electron.* **2016**, *27*, 6474–6479. [\[CrossRef\]](#)
- Barnhart, J. Occurrences, uses, and properties of chromium. *Regul. Toxicol. Pharmacol.* **1997**, *26*, S3–S7. [\[CrossRef\]](#) [\[PubMed\]](#)
- Bodke, M.R.; Purushotham, Y.; Dole, B.N. Crystallographic and optical studies on Cr doped ZnS nanocrystals. *Cerâmica* **2014**, *60*, 425–428. [\[CrossRef\]](#)
- Linga Reddy, E.; Karuppiiah, J.; Renken, A.; Kiwi-Minsker, L.; Subrahmanyam, C. Kinetics of the decomposition of hydrogen sulfide in a dielectric barrier discharge reactor. *Chem. Eng. Technol.* **2012**, *35*, 2030–2034. [\[CrossRef\]](#)
- Kogelschatz, U.; Eliasson, B.; Egli, W. Dielectric-barrier discharges. Principle and applications. *Le J. De Phys. IV* **1997**, *7*, C4–C47. [\[CrossRef\]](#)
- Bodke, M. Synthesis and characterization of chromium doped zinc sulfide nanoparticles. *Open Access Libr. J.* **2015**, *2*, 1. [\[CrossRef\]](#)
- Palma, V.; Cortese, M.; Renda, S.; Ruocco, C.; Martino, M.; Meloni, E. A review about the recent advances in selected nonthermal plasma assisted solid–gas phase chemical processes. *Nanomaterials* **2020**, *10*, 1596. [\[CrossRef\]](#)
- Bhat, V.S.; Tilakraj, T.S.; Patil, M.K.; Pujari, V.; Inamdar, S.R. One-Pot Synthesis of Biocompatible Glycine Protected Chromium Doped ZnS Nanoparticles and their Optical Properties. In *IOP Conference Series: Materials Science and Engineering*; IOP Publishing: Bristol, UK, 2022; Volume 1221, p. 012029.
- Dake, D.V.; Raskar, N.D.; Mane, V.A.; Sonpir, R.B.; Stathatos, E.; Asokan, K.; Babu, P.D.; Dole, B.N. Exploring the role of defects on diverse properties of Cr-substituted ZnS nanostructures for photocatalytic applications. *Appl. Phys. A* **2020**, *126*, 1–15. [\[CrossRef\]](#)
- Amaranatha Reddy, D.; Murali, G.; Vijayalakshmi, R.P.; Reddy, B.K.; Sreedhar, B. Effect of Cr doping on the structural and optical properties of ZnS nanoparticles. *Cryst. Res. Technol.* **2011**, *46*, 731–736. [\[CrossRef\]](#)
- Mohammed, B.A.; Ahmed, L.M. Improvement the Photo Catalytic Properties of ZnS nanoparticle with Loaded Manganese and Chromium by Co-Precipitation Method. *J. Glob. Pharma Technol.* **2018**, *10*, 129–138.
- Batra, V.; Kotru, S.; Varagas, M.; Ramana, C.V. Optical constants and band gap determination of Pb_{0.95}La_{0.05}Zr_{0.54}Ti_{0.46}O₃ thin films using spectroscopic ellipsometry and UV–visible spectroscopy. *Opt. Mater.* **2015**, *49*, 123–128. [\[CrossRef\]](#)
- Kaur, P.; Kumar, S.; Singh, A.; Rao, S.M. Improved magnetism in Cr doped ZnS nanoparticles with nitrogen co-doping synthesized using chemical co-precipitation technique. *J. Mater. Sci. Mater. Electron.* **2015**, *26*, 9158–9163. [\[CrossRef\]](#)
- Ramasamy, V.; Praba, K.; Murugadoss, G. Synthesis and study of optical properties of transition metals doped ZnS nanoparticles. *Spectrochim. Acta Part A: Mol. Biomol. Spectrosc.* **2012**, *96*, 963–971. [\[CrossRef\]](#) [\[PubMed\]](#)
- Reddy, D.A.; Divya, A.; Murali, G.; Vijayalakshmi, R.P.; Reddy, B.K. Synthesis and optical properties of Cr doped ZnS nanoparticles capped by 2-mercaptoethanol. *Phys. B Condens. Matter* **2011**, *406*, 1944–1949. [\[CrossRef\]](#)
- Choi, B.; Shim, H.; Allabergenov, B. Red photoluminescence and blue-shift caused by phase transformation in multilayer films of titanium dioxide and zinc sulfide. *Opt. Mater. Express* **2015**, *5*, 2156–2163. [\[CrossRef\]](#)
- Wang, Z.; Cao, S.W.; Loo, S.C.J.; Xue, C. Nanoparticle heterojunctions in ZnS–ZnO hybrid nanowires for visible-light-driven photocatalytic hydrogen generation. *Cryst. Eng. Comm.* **2013**, *15*, 5688–5693. [\[CrossRef\]](#)

29. Irfan, M.; Shukrullah, S.; Naz, M.Y.; Ahmad, I.; Shoukat, B.; Legutko, S.; Alsaiani, M.A. Si/SiO₂/Al₂O₃ Supported Growth of CNT Forest for the Production of La/ZnO/CNT Photocatalyst for Hydrogen Production. *Materials* **2022**, *15*, 3226. [[CrossRef](#)] [[PubMed](#)]
30. Irfan, M.; Ahmad, I.; Shukrullah, S.; Hussain, H.; Atif, M.; Legutko, S.; Petru, J.; Hatala, M.; Naz, M.Y.; Rahman, S. Construction of 0D/2D Schottky Heterojunctions of ZnO and Ti₃C₂ Nanosheets with the Enriched Transfer of Interfacial Charges for Photocatalytic Hydrogen Evolution. *Materials* **2022**, *15*, 4557. [[CrossRef](#)]
31. Ahmad, I.; Shukrullah, S.; Naz, M.Y.; Ahmad, M.; Ahmed, E.; Liu, Y.; Hussain, A.; Iqbal, S.; Ullah, S. Recent advances and challenges in 2D/2D heterojunction photocatalysts for solar fuels applications. *Adv. Colloid Interface Sci.* **2022**, *304*, 102661. [[CrossRef](#)]
32. Liang, W.J.; Fang, H.-P.; Li, J.; Zheng, F.; Li, J.X.; Jin, Y.Q. Performance of non-thermal DBD plasma reactor during the removal of hydrogen sulfide. *J. Electrostat.* **2011**, *69*, 206–213. [[CrossRef](#)]
33. Xing, C.; Zhang, Y.; Yan, W.; Guo, L. Band structure-controlled solid solution of Cd_{1-x} Zn_xS photocatalyst for hydrogen production by water splitting. *Int. J. Hydrogen Energy* **2006**, *31*, 2018–2024. [[CrossRef](#)]
34. Reddy, E.L.; Biju, V.M.; Subrahmanyam, C. Production of hydrogen and sulfur from hydrogen sulfide assisted by nonthermal plasma. *Appl. Energy* **2012**, *95*, 87–92. [[CrossRef](#)]
35. Hu, J.S.; Ren, L.L.; Guo, Y.G.; Liang, H.P.; Cao, A.M.; Wan, L.J.; Bai, C.L. Mass production and high photocatalytic activity of ZnS nanoporous nanoparticles. *Angew. Chem. Int. Ed.* **2005**, *44*, 1269–1273. [[CrossRef](#)]
36. Chivers, T.; Lau, C. The use of thermal diffusion column reactors for the production of hydrogen and sulfur from the thermal decomposition of hydrogen sulfide over transition metal sulfides. *Int. J. Hydrogen Energy* **1987**, *12*, 561–569. [[CrossRef](#)]
37. Kalamaras, C.M.; Efstathiou, A.M. Hydrogen production technologies: Current state and future developments. In *Conference Papers in Science*; Hindawi: London, UK, 2013; Volume 2013.
38. Zhao, L.; Wang, Y.; Wang, A.; Li, X.; Song, C.; Hu, Y. Cr-doped ZnS semiconductor catalyst with high catalytic activity for hydrogen production from hydrogen sulfide in non-thermal plasma. *Catal. Today* **2019**, *337*, 83–89. [[CrossRef](#)]